Cosmic Ray Variation Lags behind Sunspot Number due to the Late Opening of Solar Magnetic Field

Yuming Wang,[1, 2, 3] Jingnan Guo,[1, 2] Gang Li,[4] Elias Roussos,[5] and Junwei Zhao[6]

[1]*CAS Key Laboratory of Geospace Environment, School of Earth and Space Sciences, University of Science and Technology of China, Hefei 230026, China*

[2]*CAS Center for Excellence in Comparative Planetology, University of Science and Technology of China, Hefei 230026, China*

[3]*Mengcheng National Geophysical Observatory, University of Science and Technology of China, Mengcheng 233500, China*

[4]*Department of Space Science and CSPAR, The University of Alabama in Huntsville, Alabama, USA*

[5]*Max Planck Institute for Solar System Research, Goettingen, Germany*

[6]*W. W. Hansen Experimental Physics Laboratory, Stanford University, Stanford, USA.*

ABSTRACT

Galactic cosmic rays (GCRs), the highly energetic particles that may raise critical health issues of astronauts in space, are modulated by solar activity with their intensity lagging behind the sunspot number (SSN) variation by about one year. Previously, this lag has been attributed to result of outward convecting solar wind and inward propagating GCRs. However, the lag's amplitude and its solar-cycle dependence are still not fully understood (e.g., Ross & Chaplin 2019). By investigating the solar surface magnetic field, we find that the source of heliospheric magnetic field, i.e., the open magnetic flux on the Sun, already lags behind SSN before it convects into heliosphere along with the solar wind, and the delay during odd cycles is longer than that during sequential even cycles. Thus, we propose that the GCR lag is primarily due to the greatly late opening of the solar magnetic field with respect to SSN, though solar wind convection and particle transport in the heliosphere also matters. We further investigate the origin of the open flux from different latitudes of the Sun and found that the total open flux is significantly contributed by that from low latitudes where coronal mass ejections frequently occur and also show an odd-even cyclic pattern. Our findings challenge existing theories, and may serve as the physical basis of long-term forecasts radiation dose estimates for manned deep-space exploration missions.

1. INTRODUCTION

Galactic Cosmic Rays (GCRs), which are omnipresent, charged and energetic particles coming from outside of the heliosphere, are affected by the heliospheric magnetic flux as they propagate inward from the heliospheric boundary at about 120 AU (Krimigis et al. 2013). Enhanced magnetic flux is

Corresponding author: Yuming Wang & Jingnan Guo
ymwang@ustc.edu.cn, jnguo@ustc.edu.cn

more efficient in preventing GCRs from deeply penetrating into the heliosphere, causing decrease of GCR fluxes towards solar maxima. Thus, the GCR flux is generally anti-correlated with solar activity following the quasi-11-year solar cycle (e.g., Potgieter 1998). The variation of GCR fluxes at Earth has been correlated with various solar and heliospheric parameters, such as the Sunspot Number (SSN), the strength and turbulence level of heliospheric magnetic field (HMF), the heliospheric current sheet (HCS) tilt angle, the open solar magnetic flux, the solar polarity, etc. (Usoskin et al. 1998; Cliver & Ling 2001; Rouillard & Lockwood 2004; Alanko-Huotari et al. 2007; Potgieter 2013), and empirical correlations have been proposed.

In particular, when correlating the GCR and SSN temporal variations, the strongest anti-correlation appears when the GCR profile is shifted backward in time, suggesting a delay of the GCR variation with respect to the solar activity evolution. The classic picture to explain this time lag involves the solar wind convection and the GCR transport in the heliosphere (Parker 1965; Van Allen 2000; Dorman 2001; Usoskin et al. 2001; Cliver & Ling 2001; Thomas et al. 2014). I.e., GCRs propagate inward throughout the heliosphere and are affected by the magnetic field carried by the outward solar wind during their journey. Meanwhile, different paths of GCRs during different phases of the solar cycle could also influence the arrival times of GCRs.

It has also been observed that the modulation of GCRs has an odd-even cycle dependency (Webber & Lockwood 1988; Van Allen 2000; Cliver & Ling 2001; Thomas et al. 2014), i.e., the GCR-SSN lag is much longer (one year or more) during odd solar cycles than that (no more than two months) during even solar cycles. This has been explained, following the above theory of the cause of the delay, by the different drift patterns and diffusion process of GCR propagation through the heliosphere when the solar magnetic poles have predominantly positive or negative spatial orientation following the 22-year Hale cycle (Jokipii et al. 1995, 1977; Ferreira & Potgieter 2004). Specifically speaking, the polarity of the solar field (often represented by symbol A) is positive/negative when the dominant polar field is outward/inward in the northern hemisphere. The polar field reversal occurs around the time when SSN reaches maximum and divides each solar cycle into A+ and A- half cycles. Influenced by the curvature and gradient drift pattern, GCR protons arrive at the inner heliosphere after approaching the solar poles and moving out along the heliospheric current sheet during A+ phase. In opposition, during A- phase, GCR protons propagate inward along the HCS plane and leave via the poles. Around solar maximum, disturbances in the solar wind are much stronger making it more difficult for particles to propagate inward along the HCS plane. Odd solar cycles start with A+ polarity and switch to A- so that GCRs experience a slower recovery during the declining phase of the cycle when they predominantly enter the heliosphere along the HCS. Even cycles (first A- and then A+) experience a faster GCR recovery.

However, the above GCR transport model alone can hardly predict the GCR-SSN lags at the precision of a few months to which the magnitude of these lags is evaluated from observations. Recent study (Ross & Chaplin 2019) has shown that during Cycle 24 GCR-SSN lag is slightly longer than preceding even-numbered cycles, although not as high as observed in previous odd-numbered cycles. To explain such exceptions, theoretical models would need to rely on various ad-hoc and adjustable parameters whose values can not be directly verified but are chosen to fit the modeling results with observations.

In this study, we focus on the solar open field (OF) that forms the large-scale HMF where the GCRs propagate through. Via a thorough investigation of GCR-SSN correlation and the OF-SSN

correlation throughout several solar cycles and at various heliospheric distances, we find that the temporal evolution of GCRs is closely mirroring the temporal variations of the open field which is already delayed with respect with SSN. Thus, we propose that the GCR-SSN lag is primarily due to the late opening of the solar magnetic field at the Sun while solar wind convection and GCR transport probably make a secondary contribution to cause a longer delay on top of the OF-SSN delay. Besides, we show that the OF-SSN delay already has an odd-even cycle dependency, or more precisely speaking, the OF-SSN delay during odd cycles is longer than that during its sequential even cycles, that could be the main driver of the odd-even cycle dependence of the GCR-SSN delay. We further investigate the origin of the OF from different latitudes of the Sun and found that the total OF is largely contributed by that from low latitudes where CMEs are frequently launched from active regions and also show an odd-even cycle dependency as GCR-SSN delay. These findings advance our understanding on the solar cycle evolution and its impact on the heliosphere.

2. GCR DELAYS AT VARIOUS HELIOCENTRIC DISTANCES
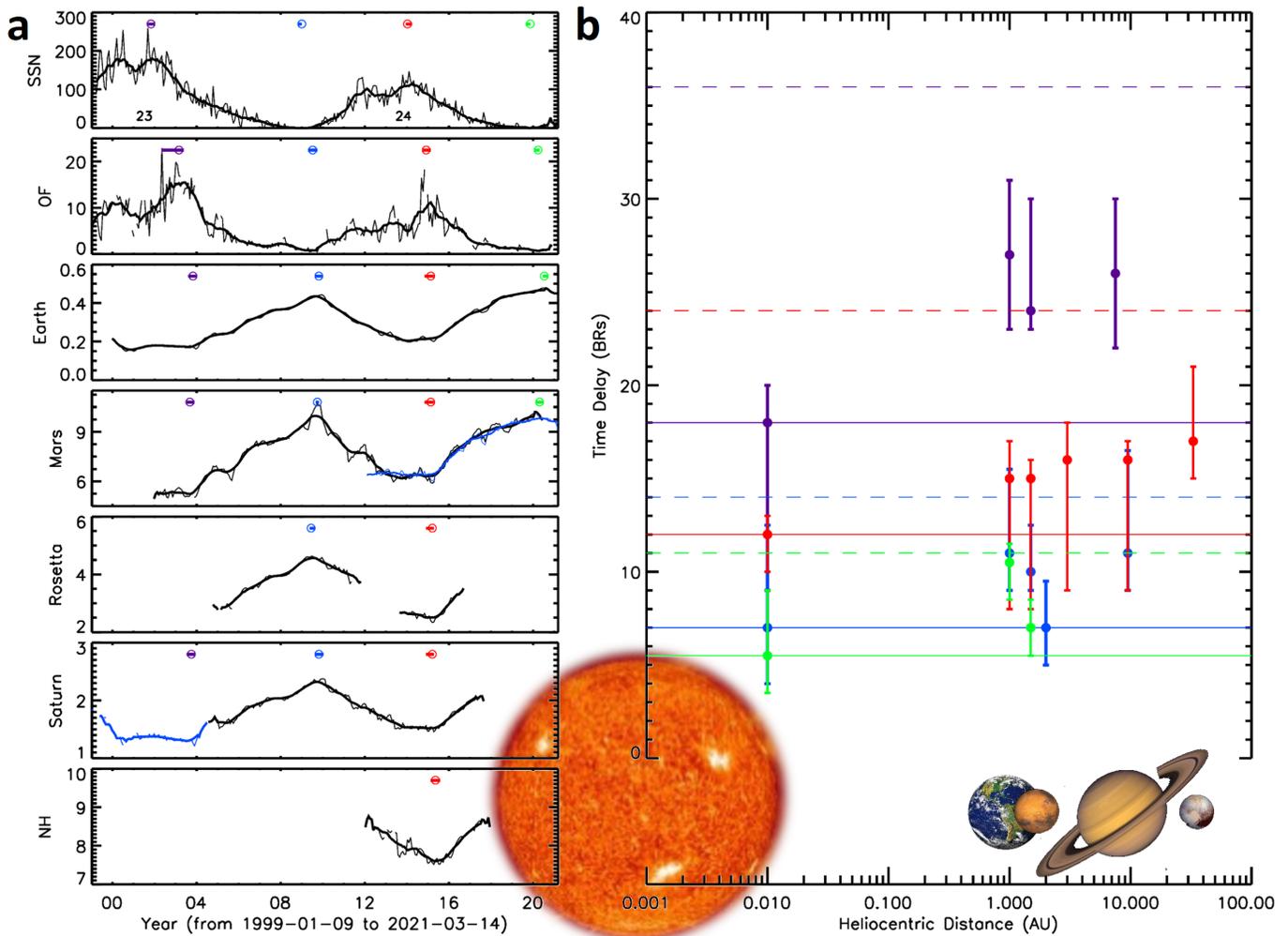
Figure 1. Time delays of solar open flux and GCR fluxes at five different heliocentric distances with respect to the SSN variation for Solar Cycles 23 and 24. (a) From the top to bottom, the panels show the solar cycle variations of the SSN (Clette et al. 2014, version 2.0), the open magnetic flux on the Sun (in units of $\times 10^{13}$ Wb, derived from the CSSS model (Zhao & Hoeksema 1995) based on the WSO magnetic synoptic charts (Duvall et al. 1977), see the main text for details), the GCR flux at Earth (measured by the EPHIN (Müller-Mellin et al. 1995) onboard the Solar and Heliospheric Observatory (SOHO, Domingo et al. 1995) of protons above 53 MeV), the GCR flux at Mars (~ 1.5 AU, measured by HEND (Boynton et al. 2004) onboard Odyssey orbiter of the Martian albedo neutrons with energies 10 eV – 1 MeV in black and by RAD (Hassler et al. 2012, 2014) onboard the Curiosity rover of the Mars's surface dose rates induced by original protons above $\sim$160 MeV in blue (Guo et al. 2018)), the GCR flux within 4.5 AU (measured by SREM (Evans et al. 2008) onboard the Rosetta spacecraft of ions above 49 MeV), the GCR flux near Saturn at about 9.5 AU (measured by Cassini spacecraft of ions above 120 MeV (Roussos et al. 2020); cruise data are shown in blue until Cassini arrived at Saturn in 2004 July) and the GCR flux from about 22 AU to 40 AU measured by New Horizon (of 120 MeV – 1.4 GeV ions (Hill et al. 2020)). The GCR flux recorded by New Horizon is in units of $\#/\text{keV}/\text{cm}^2/\text{sr}/\text{sec}$; the GCR data of RAD are scaled by 32μGy/day and the GCR fluxes from other instruments are all in the units of the counts per seconds. The temporal resolution of all the data is one BR as shown by the thin curves. The thick curves are obtained after the running smooth using a 13-BR window. The purple, blue, red and green circles in the first panel mark the four selected extrema (either maximum or minimum) of the SSN, and the circles in the other panels mark the positions of the corresponding extrema of the data shown. The horizontal bars across the circles give the uncertainties. (b) The dots give the time delays for the extrema with the same colors, and the error bars are just the horizontal bars in (a). The solar distance of the open flux is set at 0.01 AU, which is close the cusp surface in the CSSS model where the solar magnetic fields open into heliosphere. The horizontal solid lines mark the open flux delay times of the four extrema, and the dashed lines mark two times of the corresponding delay times.

To clearly show the GCR delay in the heliosphere, we investigate the energetic particle measurements at Earth, Mars, Rosetta swinging around 3 AU, Cassini near Saturn and New Horizon approaching Pluto during Cycles 23 and 24 (see Fig.1a and Appendix A for the description of the GCR data). We also use the daily SSNs (Clette et al. 2014) which are directly obtained from the SIDC of Royal Observatory of Belgium (http://www.sidc.be/silso/datafiles; the latest version 2.0 is used). All of these data are prepared in each Bartels rotation (BR, one BR is 27 days) by calculating the median value of the daily values of these data for each BR.

First, we use the peak-alignment method to estimate the GCR time delays with respect to SSN at various distances. In this method, we first locate a notable extremum (maximum or minimum) in SSN, and then set a reasonable time range to search the corresponding extremum in the parameter of interest, e.g., the GCR flux at Earth. The time difference between the two peaks is the time delay. A positive value means the delay and a negative value the lead. Since short-term fluctuations due to temporary solar transients may influence the positions of the extrema, we smooth the data over a certain size and repeat the above procedures to obtain the time delay again. We change the smoothing window from one BR to 13 BRs, close to one year, and get 13 peak locations for each parameters as well as 13 time delays, of which the median value is adopted as the final time delay (the color circles or dots in Fig.1) and the minimum and maximum values are used as the uncertainty (the associated bars in Fig.1).

We select four SSN extrema (two maxima and two minima, the color-coded circles in Fig.1a) during Cycles 23 and 24 for the peak-alignment method. It should be noted that during the cycle maxima,

SSN depicts a clear double-peak structure (see the top panel of Fig.1a), and the second peak of the SSN around a solar maximum is used in this study to make sure that we have as many extremum values as possible across different datasets which cover various durations (other panels of Fig.1a).

The estimated GCR delays are summarized in Fig.1b, which shows that the GCR delay is generally longer during solar maxima than minima, and could be as long as more than 22 solar BRs or 1.6 years. According to existing particle transport theories (e.g., Potgieter 2013), such delays are thought to be mainly due to the outward convection of solar cycle conditions of the HMF with the solar wind and the inward diffusive propagation of GCRs. Here, we look at this issue from another angle of view. We go to the source of the HMF, i.e., the open magnetic field on the Sun, to see if the delay in respect to SSN already happens before the solar wind outward convection, which may provide an alternative explanation.

Since there is no technique to directly observe solar open field, we use the current-sheet source-surface model (CSSS, Zhao & Hoeksema 1995) to extrapolate and locate the open magnetic fields based on the line-of-sight (LOS) photospheric magnetic fields observed by Wilcox Solar Observatory (WSO, Duvall et al. 1977, http://wso.stanford.edu/synopticl.html). The WSO synoptic charts are stored in Carrington rotations. To obtain the synoptic charts in Bartels rotations, we shift the starting time of the charts and reassemble them. Here, we use WSO data rather than the data from the Michelson Doppler Imager (MDI, Scherrer et al. 1995) onboard the SOHO spacecraft and the Helioseismic and Magnetic Imager (HMI, Hoeksema et al. 2014) onboard the Solar Dynamics Observatory (SDO, Pesnell et al. 2012) because WSO data cover the past four solar cycles, much longer than the MDI or HMI data. The difference of the extrapolation results between them and the influence on our conclusion could be found in Appendix B.

The CSSS model is a widely-used coronal magnetic field extrapolation model (e.g., Wang & Zhang 2007; Gui et al. 2011), and compared to the potential field source surface (PFSS) model, it includes the effects of the large-scale horizontal current sheet in the inner corona, the warped heliospheric current sheet in the upper corona and the volume currents in the outer corona, and can predict the strength and polarity of HMF better (Zhao & Hoeksema 1995). Using this model, we calculate the spherical harmonic coefficients up to 9 orders, and trace magnetic field lines from the solar surface. Field lines returning back to the surface are closed field lines, while those crossing over the cusp surface at 2.5 solar radii are open field lines. Since spatial resolution of the input WSO chart is 72 (in longitude) by 30 (in latitude), we trace one field line from each grid point resulting in a total of $72 \times 30 = 2160$ field lines. Meanwhile, we calculate the surface area of each grid point. The total area of all the grid points is the total solar surface area. With this information, we can easily derive the open flux, open area and the averaged open magnetic field strength. It should be noted that there are sometimes missing data in WSO LOS synoptic charts. If the number of missing data points exceeds 60, i.e., about 3% of total number of data points, in a BR chart, we simply omit the open field data corresponding to this BR chart.

We find that the total flux of the open fields shows clear solar cycle variations (the second panel of Fig.1a) and looks well anti-correlated with the GCR fluxes. Using the previous peak-alignment method, we determine the time delay of the open flux after the SSN to be about 18, 8.5, 12 and 5.5 BRs for the four extrema, respectively, as summarized in Fig.1b. The time delay of each GCR dataset is longer than the delay of the corresponding open flux, except for the distance-varying Rosetta data point in blue. Considering that the GCR delay may consists of two sources: one is the process in

the heliosphere including the heliospheric magnetic field convection by solar wind and the particle transport, and the other is at the very beginning on the Sun, i.e., the delay of the solar open flux, we can find in the figure that the latter may play an important role as none of the estimated GCR delays is longer than two times of the corresponding open flux delay within the orbit of Pluto (indicated by dashed lines in Fig.1b).

3. GCR DELAYS AT EARTH OVER THE PAST 45 YEARS

We further extend the analysis to the past 45 years since 1976 (Cycles 21-24) as shown in Fig.2a, during which the WSO observations of the solar photospheric magnetic fields are available but continuous GCR observations are only available at Earth by ground-based neutron monitors. We use the Oulu (Usoskin et al. 2005) data for this study. Previous studies show that the delay time can be energy-dependent with shorter delays for higher energy GCRs (Shen et al. 2020), an effect which may be attributed to the energy-dependent transport of GCRs in the heliosphere (Moloto & Engelbrecht 2020). Compared to the SOHO/EPHIN data in Fig.1a, the GCR delay time at Earth is about one to two BRs shorter if the Oulu is used (more details in Appendix A and Fig.A1).

Using the same peak-alignment method, we select the second major maximum (to keep the consistency with what we did for Cycles 23 and 24) of each cycle and every solar minimum, resulting in a total of 8 extrema (the top panel of Fig.2a), to find the delay of each corresponding extremum in the solar open flux and the GCR flux (the last two panels of Fig.2a). The results displayed by color dots with error bars in Fig.2b show that for all the extrema, the GCR delays were roughly equal to or slightly longer than the corresponding open flux delays and were much shorter than two times of the open flux delays, suggesting that the primary role of the open flux in causing the GCR delay holds for the previous four solar cycles. We note that the purple point numbered as 21 (the solar minimum between Cycles 21 and 22) is an exception with the GCR delay much longer. However, the large uncertainties in both time delays make it difficult to discuss about this outlier.

Benefiting from the continuous collection of GCR data at Earth throughout this period, we employ the cross-correlation method to reveal the cycle variation of the delay time. For any given time, we first select a N-year wide segment centering at this time in SSN, and then set the same wide time window on the parameter of interest, e.g., the open flux or the GCR flux, to calculate the correlation coefficient (cc) between the selected segments of the parameter and the SSN. The N-year window rolls through the parameter over a reasonable time range to make sure of locating the best correlation within the range. The time delay is the shifted time of the window away from its original position. Meanwhile the associated cc value is also obtained. Since the correlation depends on the size of the time window, we change the value of N from 5 to 11 by a step of 0.074 (i.e., one BR), gathering the data of half of a solar cycle to a complete solar cycle, and repeat the above steps to achieve a total of 82 time delays and cc values, among which the time delays associated with a cc less than 0.5 are discarded. The median values of these delays and these cc values are chosen as the final time delay and the final cc value, respectively. The 20th/80th percentile is chosen as the uncertainty range of the time delay. Applying the above technique to the data throughout Solar Cycles 21-24, we then get the cycle variations of the time delays as shown by the color-coded ribbons in Fig.2a.

The smoothness of the data has little influence on the result of the cross-correlation analysis. The color-coded ribbons in Fig.2a are obtained based on the 13-BR smoothed data, and those in Fig.3a based on the unsmoothed data. They look similar at the scale of solar cycle. The percentage of the data points with the GCR delay longer than or equal to the open flux delay is 79%, similar to that
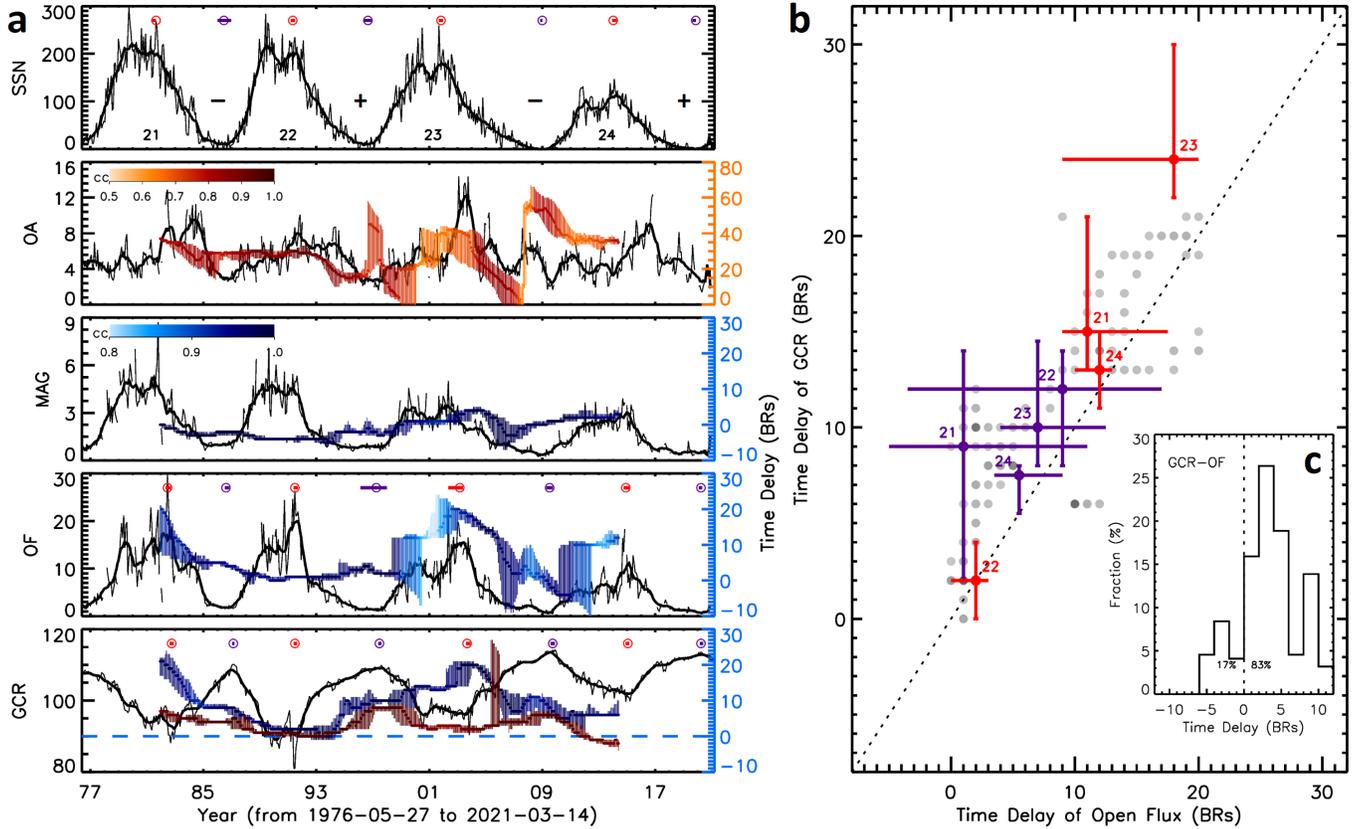
Figure 2. Time delays of the open magnetic field area, open field strength, open flux on the Sun and GCR fluxes at Earth with respect to the SSN evolution for the previous four solar cycles. (a) From the top to bottom, the panels show the solar cycle variations of the SSN, open area (in units of % of total solar surface, TSS), open field strength (in units of Gauss), open flux on the Sun and the GCR flux at Earth (Oulu, counts/sec), respectively. Same as Fig.1a, the circles and crossing bars are the selected extrema and their uncertainties. The red ones are for the second major maximum of each cycle and the purple ones for the solar minima. The color-coded ribbon-like curves in the second through the fifth panels show the solar cycle variations (from 1981 Dec. 12 to 2014 May 26) of the time delays of the shown parameter relative to the SSN by using cross-correlation analysis on the 13-BR smoothed data. These ribbons are composed of dots (the median values of the time delays) and error bars (the 20th/80th percentiles of the time delays), scaled by the right y-axis of each panel. The colors of the ribbons represent the correlation coefficients, scaled by the color bars in the second and third panels. (b) The red and purple dots with error bars mark the time delays of the open flux and GCRs for the 8 extrema. The solar cycle numbers are also indicated. The gray dots show all the time delays obtained from the cross-correlation analysis. Multiple data points with the same time delays result in a darker dot. The dotted line is the diagonal line. (c) The histogram shows the distribution of the difference between the GCR delays and the open flux delays based on the cross-correlation analysis, i.e., the distribution of the gray dots in (b). For about 78% of the data points, the GCR delay is longer than the open flux delay.

based on the smoothed data, which is 83%. But we also notice that the smoothness of the data is probably an error source for few gray dots in Fig.2b and Fig.3b, of which the GCR delays are shorter than the open flux delay. For example, comparing the red color-coded ribbons in the last panels of Fig.2a and Fig.3a, we find that during 2013 – 2014, the GCR flux seems to evolve ahead of the open
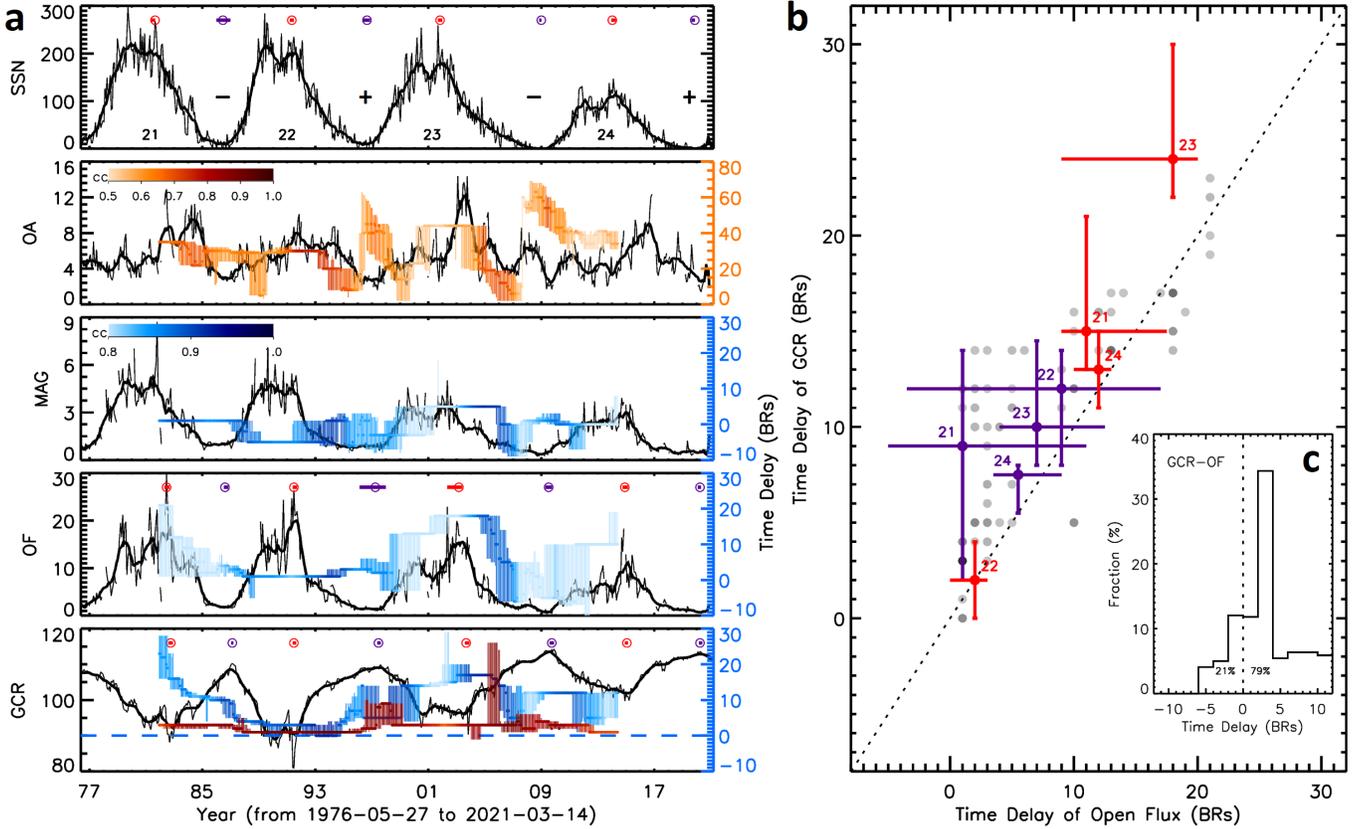
Figure 3. The same as Fig.2 except the data used for <u>cross-correlation analysis are not smoothed.</u>

flux in Fig.2a, but behind of the open flux in Fig.3a. This illustrates the uncertainty caused by the smoothness of the data sets.

We obtain the cycle evolution of the delays as shown by the color-coded ribbons in the last two panels of Fig.2a. Especially, the red color-coded ribbon in the last panel lying below the blue color-coded ribbon suggests that the GCR delays with respect to SSN are longer than the GCR delays with respect to the open flux. The gray dots in Fig.2b further show that about 83% of the GCR delays are longer than or equal to the open flux delays, and if we only choose the delays with the correlation coefficient ≥ 0.9, the fraction increases to 93% (not shown in the figure), supporting again that open flux delay is the main driver for the corresponding GCR lags.

Meanwhile, we find that the open flux delays during the odd cycles were notably longer than the delays during the sequential even cycles (see the blue color-coded ribbon in the second last panel of Fig.2a or Fig.3a). The similar odd-even pattern was observed in the GCR delays with respect to SSN (Van Allen 2000; Cliver & Ling 2001; Thomas et al. 2014), but does not appear in the GCR delays with respect to the open flux (see the ribbons in the last panel of Fig.2a or Fig.3a). Thus, the open flux delays could also be a driver of the observed odd-even cycle behavior in the GCR lags, that has been soly attributed to the different drift patterns of GCR propagation through the heliosphere following the 22-year Hale cycles, i.e., GCRs drift in through the poles during A+ cycle or along the HCS close to the ecliptic plane during A- cycle as previously studied (Jokipii et al. 1995; Ferreira
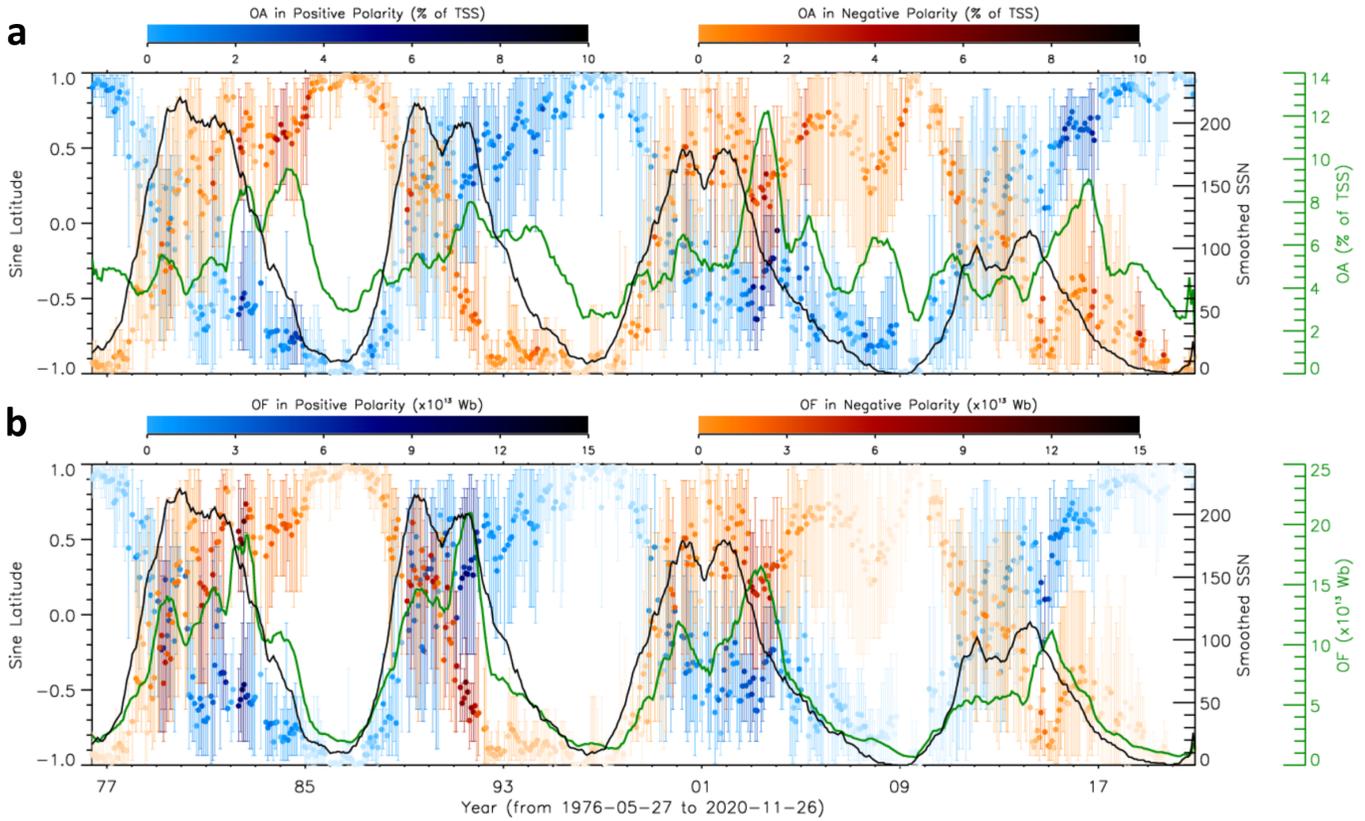
Figure 4. Cyclic diagrams of the solar open area and open flux. **(a)** The latitudinal and size evolution of the open area with the solar cycles. The blue/red dots indicate the latitudinal centroid of the positive/negative open field lines. The darker the color, the bigger the total area, which is scaled by the color bars on top of the panel. The error bars give the 20th/80th percentile of the open field lines in latitude. The smoothed SSN (black curve) and total open area (green curve) are overplotted. **(b)** Similar to **(a)**, but for the open flux.

& Potgieter 2004; Potgieter 1998, 2013). According to the analysis here, the drift effect due to the solar polarity changes is perhaps only a secondary effect in driving the global variation of GCRs.

### 4. ORIGIN OF THE OPEN FLUX DELAY ON THE SUN

To further find out the origin of the delay of the open flux variation with respect to SSN variation, we investigate the averaged magnetic field strength and the area of the solar open fields (the second and third panels of Fig.2a or Fig.3a), whose product is the open magnetic flux. Using the same cross-correlation analysis, we find that the strength of the open magnetic field changes with the SSN almost synchronously with a small delay varying between ±3 BRs (the blue-coded curve), but the open area lags behind the SSN substantially by about 31 BRs or 2.3 years on average, sometimes by more than 40 BRs corresponding to 3 years (see the red-coded curve). Such great delays of the open area cause the open flux to significantly lag behind the SSN. Note that the delay of open area around the solar minimum between Cycles 23 and 24 changed abruptly. This segment is not reliable, because during that period there were multiple local maxima and minima even in the smoothed open area data, making it difficult to determine a unique association between the SSN minimum and the open area minima.
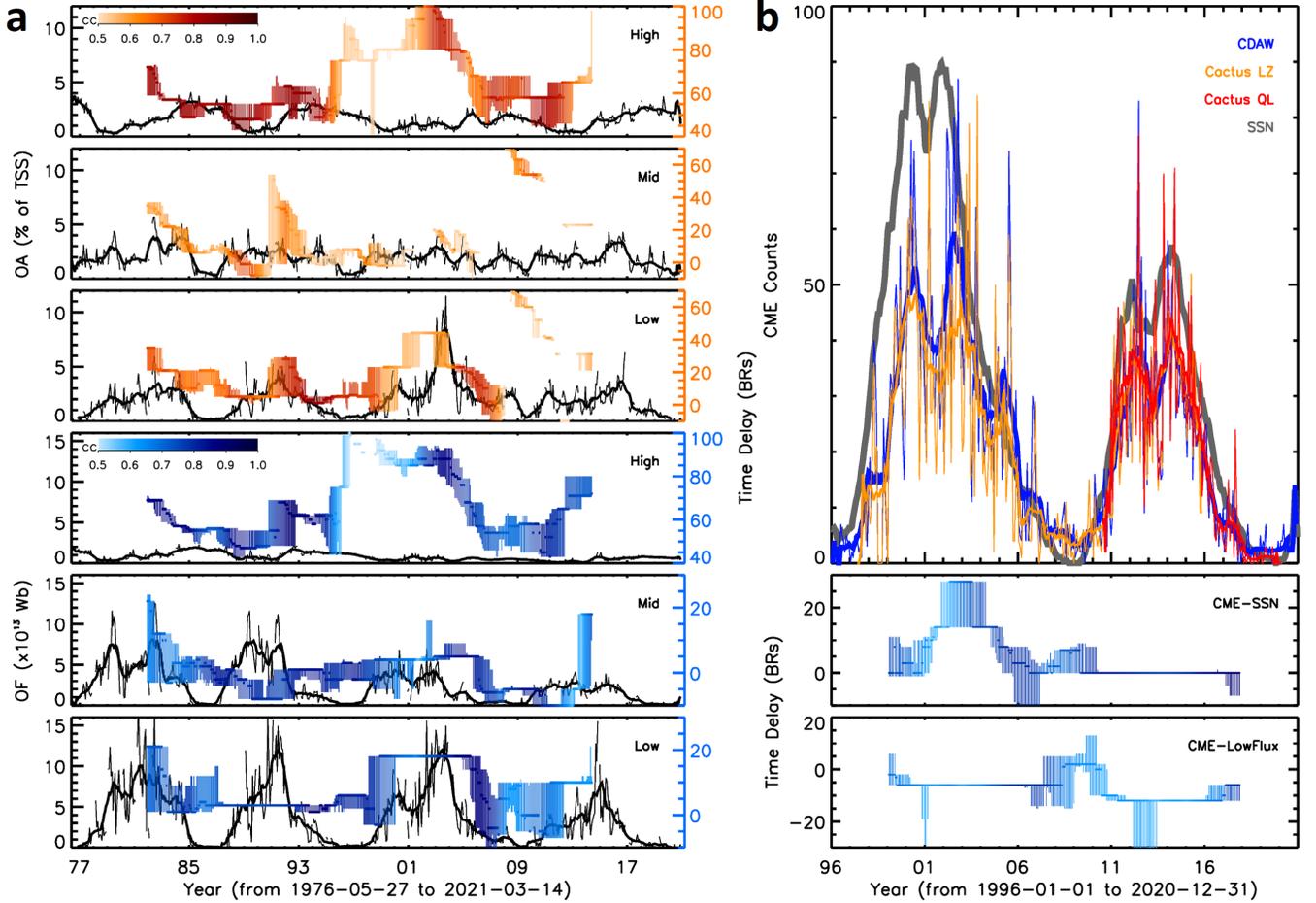
Figure 5. Solar cycle variations of the high, mid and low latitudinal open fields and the CME occurrence. (a) From top to bottom are the open areas at the high (beyond ±60°), mid (between ±30° and ±60°) and low (within ±30°) latitudes and the open fluxes at the the high, mid and low latitudes. The color-coded ribbons have the same meaning as those in Fig.2a, showing the delays relative to the SSN. (b) The top panel shows the number of CMEs per BR with a speed larger than 500 km s^{-1}. Thin curves are the original counts and thick ones are the 13-BR smoothed values. CME counts derived from CDAW CME catalog (Yashiro et al. 2004) are indicated in blue and those from Cactus catalog (Robbrecht & Berghmans 2004) are in orange and red. The smoothed SSN is overplotted as the gray curve (value is scaled by 0.4). The bottom two panels show the time delays of the CDAW CME counts relative to the SSN and low-latitudinal open flux, respectively. The color bar in the fourth panel of (a) is used.

The detailed evolution of the open area and flux over solar cycles is shown in Fig.4a and b, respectively. The open field of positive or negative polarities appears near one polar region at solar minima, gradually migrates toward low latitudes with increasing solar activity until solar maxima, and then continuously moves to the other polar region. During the course, the latitudinal variations of the total open area and the open flux follow the SSN, but their amplitudes evolve with a lag behind the SSN and reach the maximum generally during the declining phase of each cycle.

Solar open field originates mainly from coronal holes (normally located at high latitudes, Wang et al. 1996) and sometimes from active regions (distributed at low latitudes, Schrijver & Derosa 2003). We
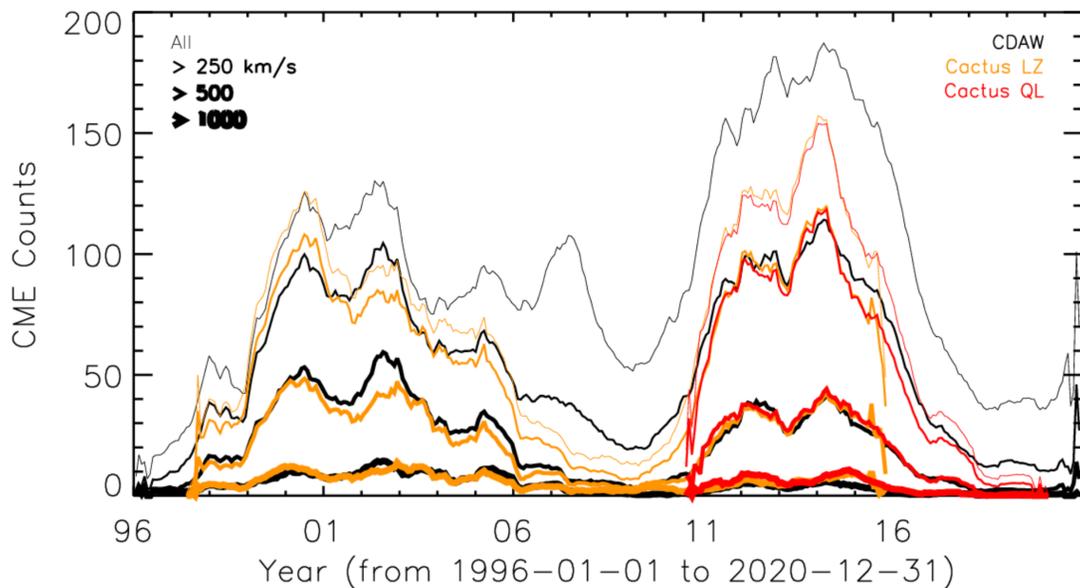
Figure 6. The solar cycle variations of the CME numbers according to the CDAW CME catalog (Yashiro et al. 2004) (black) and the Cactus catalog (Robbrecht & Berghmans 2004) based on the LASCO level zero data (orange) and on the LASCO quick look data (red). From thin to thick, the lines show the numbers of CMEs with the speed larger than 0, 250, 500 and 1000 km s^{-1}, respectively.

then investigate the open area and open flux rooted in the high-(beyond $\pm 60°$), mid-(between $\pm 30°$ and $\pm 60°$) and low-(within $\pm 30°$) latitudinal zones, as displayed in Fig.5a. It is found that the open areas in different latitudes are on the same order of magnitude. The variations of the open areas at low and mid-latitudes follow the SSN with a delay, and that in polar regions are more or less reversed in phase. Consequently, the phases of the open flux at high and low latitudes are reversed too. This can be understood by noticing that the solar open field is mainly contributed by the lowest-order of the multi-polar magnetic fields (Wang et al. 2005; Jiang et al. 2011), i.e., the axial dipole field and the equatorial dipole field that provide most of the open fluxes at high and low latitudes, respectively, with reversed phases.

The open flux at low latitudes should be paid attention as it is overall about two times of the high-latitude open flux. Considering that low latitudes are the main locations of active regions that can also contribute to the heliospheric magnetic flux through coronal mass ejections (CMEs, Luhmann et al. 1998; Owens & Crooker 2006), we check the solar cycle variation of the CME occurrence number and its relationship with the low-latitude open flux.

CMEs are continuously observed by the Large Angle and Spectrometric Coronagraph (LASCO, Brueckner et al. 1995) on board the SOHO spacecraft since 1996. There are several CME catalogs covering Cycles 23 and 24. Here we choose one manually-maintained CME catalog and one machine-automated catalog. The CDAW catalog (https://cdaw.gsfc.nasa.gov/CME_list/) is manually-maintained (Yashiro et al. 2004), and the Cactus catalog (http://sidc.be/cactus/) is based on a machine-automated algorithm (Robbrecht & Berghmans 2004) using either the level zero (LZ) data (until 2015-10-31) or the quick look (QL) data (from 2010-07-09). The CME linear speed in the LASCO field of view is provided in the CDAW catalog and the median velocity is provided in the Cactus catalog. They are mostly comparable for CMEs without significant acceleration. CME counts

with a certain speed threshold is calculated for each BR as shown in Fig.6. The comparison of the two different catalogs shows a better consistency with a larger threshold. As a result, we choose the CMEs with a speed larger than 500 km s^{-1} for analysis (Fig. 5b) as the two catalogs are consistent and the CME number is large enough.

It is remarkable that the CME occurrence rate also shows the odd-even solar cycle pattern as revealed by the cross-correlation analysis (the top and middle panels of Fig.5b), i.e., it notably lagged behind the SSN in Cycle 23, but changed synchronously with the SSN in Cycle 24. Previous studies presented a model for dynamical energy balance in the flaring solar corona which predicted a time lag between flare occurrence and the supply of energy to the corona (Wheatland & Litvinenko 2001). Studies of solar flare rates and SSN over 5 solar cycles confirmed this time delay and also found it much longer for odd solar cycles than for even cycles (Temmer et al. 2003). Both flares and CMEs represent the process of the gradual accumulation and impulsive release of the magnetic energy in the solar corona. This process may explain the flare/CME lagging behind the SSN, but not for their odd-even behaviors, which deserves further studies.

We further compare the CME numbers with open flux at low latitudes (the last panel of Fig.5b), and find that the open flux lagged behind the CME rate almost constantly, by about 6 BRs in Cycle 23 and 10 BRs in Cycle 24. This implies that part of the extrapolated solar open flux should result from the reconfigured magnetic fields after CMEs, consistent with the previous studies that up to 30% heliospheric field could come from active regions (Schrijver & Derosa 2003) and CMEs could contribute to the open solar magnetic fields (Luhmann et al. 1998). According to the time delay between CME counts and open flux in Fig.5b, we conjecture that the time scale of the eruption-driven field opening that can be reflected in the photoshperic magnetogram and the extrapolation is about half a year. This finding sheds light on the origin and opening of the solar magnetic flux at low latitudes.

5. CONCLUSION

In summary, by investigating the GCR fluxes at various heliocentric distances and the solar open flux over the previous four solar cycles, we found that the GCR-SSN delay is longer than the OF-SSN delay, and both of them show the same odd-even cyclic pattern. We further found that the open flux delay is mainly due to the significant delay of the solar magnetic field opening, and CMEs make important contributions to the open flux at low latitudes. We also showed that the frequency of CME occurrence has an odd-even cycle dependency. Considering that the solar open flux is the source of HMF, we conclude that the GCR-SSN delay has its major origin on the Sun and is dominated by the solar cycle evolution at and below the solar surface. In other words, the delay of the open flux on the Sun is the primary contributor to the GCR delay in the heliosphere, and consequently is also the major cause of the odd-even cycle pattern of the GCR delay. This finding adds a new dimension (open flux delay) to the existing theories that address the GCR-SSN delay mainly based on the solar wind convection and transport of GCRs in the heliosphere, and should be folded into existing theoretical models. The correlations established among SSN, open flux and GCR intensity in this study provide a basis for the long-term forecast of the GCR radiation levels in the heliosphere which are important concerns for future human space missions (Cucinotta et al. 2017).

APPENDIX

A. GCR DATA SETS

The GCR data at Earth in Figure 1 are measured by the Electron Proton Helium Instrument (EPHIN) which is part of the Comprehensive Suprathermal and Energetic Particle Analyzer (COSTEP, Müller-Mellin et al. 1995) on the SOHO spacecraft. As a proxy for the measurement of GCRs, we utilize the channel for particles penetrating through the last detector with minimum ion energies of 53 MeV/nuc. The GCR data at Earth in Figure 2 and 3 are measured by the neutron monitor at Oulu (Usoskin et al. 2005) and the averaged daily values are downloaded from http://cosmicrays.oulu.fi. As GCRs enter Earth's atmosphere, they collide with atmospheric particles, producing secondary particles such as neutrons, which are then observed at the detectors situated around the globe. Ground level enhancement induced by solar energetic particles (SEPs) are removed and the daily data are binned into each BR with the median values used in the following analysis. The Oulu neutron monitor has been recording data since 1964. Given the Earth's geomagnetic field and atmospheric shielding, the cut-off rigidity for Oulu is 1 GV, corresponding to about 430 MeV, much higher than that by SOHO/EPHIN. Thus, the delay time of the Oulu GCRs will be shorter than SOHO particles as illustrated in Fig.A1. The amplitude of the time shift between the two data sets is steadily one or two BRs.

The GCR data at Mars include the data from the High Energy Neutron Detector (HEND, Boynton et al. 2004) onboard the Mars Odyssey spacecraft (https://pds-geosciences.wustl.edu/missions/odyssey/grs_edr.html) and the data from the Radiation Assessment detector (RAD, Hassler et al. 2012) onboard the Curiosity Mars rover (https://pds.nasa.gov/ds-view/pds/viewDataset.jsp?dsid=MSL-M-RAD-3-RDR-V1.0). HEND measures the albedo neutrons that are generated by primary GCRs in the Martian environment and scattered upwards to the orbit. The detector with the thickest moderator layer (about 30 mm) is most sensitive to the neutrons with energies 10 eV–1 MeV and its count rate is used in this study. RAD data are the absorbed dose rate, which is the energy deposit rate by all surface GCRs (including both primary and secondary particles generated in the atmosphere) in the plastic detector. SEPs are removed from both datasets before the daily values are averaged into those for each BR (median values are used).
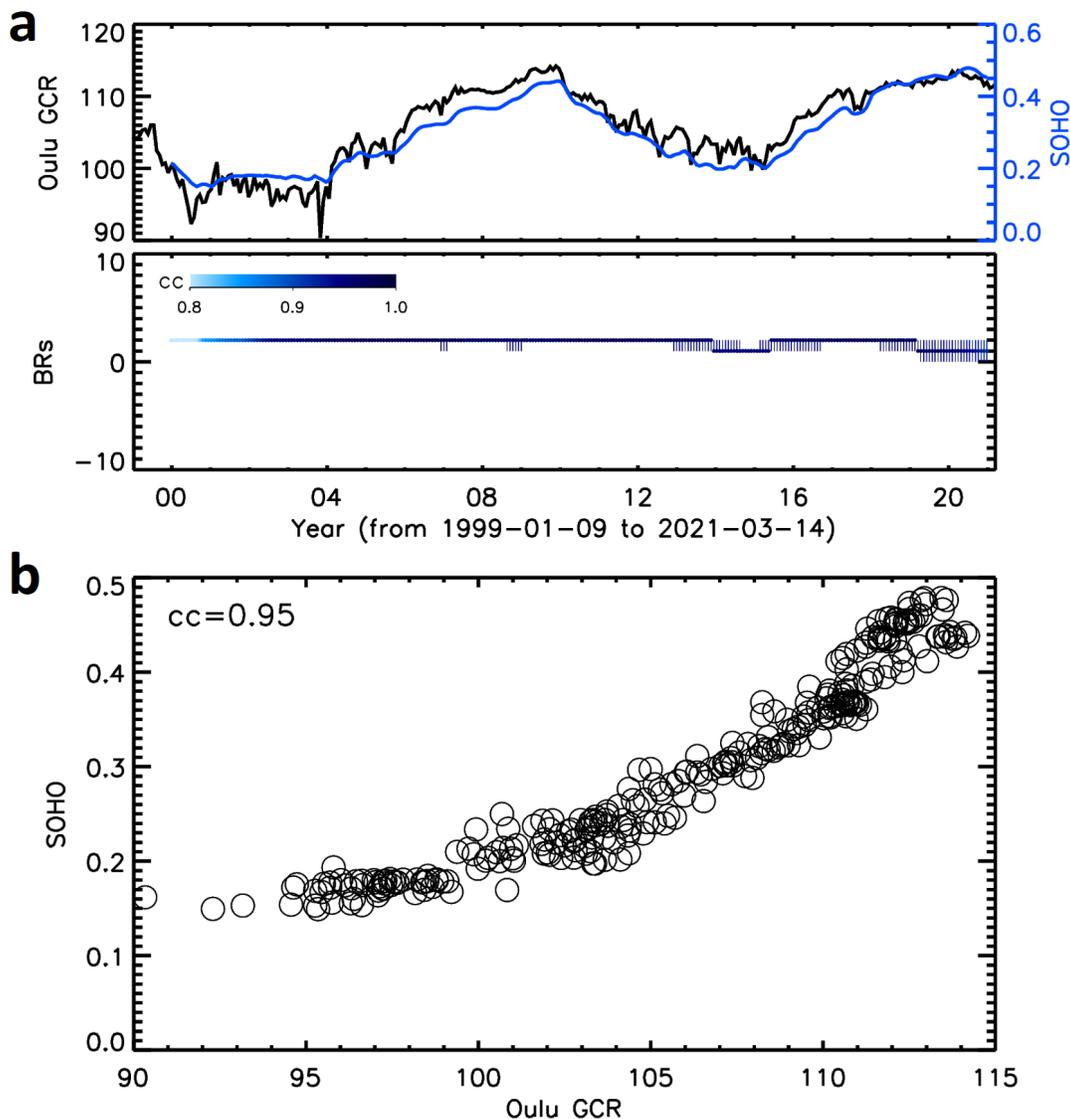
Figure A1. The upper panel of (a) shows the comparison between the BR data of the Oulu GCR flux (black) and that of the SOHO/EPHIN energetic particle flux (blue). The lower panel of (a) shows the time delay of the SOHO/EPHIN data with respect to the Oulu GCR data based on the cross-correlation analysis, with the same meaning as that shown in Fig.2a. Panel (b) shows how well the Oulu data and the SOHO/EPHIN data are correlated when 2-BR shift is applied.

The data of the Standard Radiation Environment Monitor (SREM, Evans et al. 2008) aboard the Rosetta (Glassmeier et al. 2007) are available at https://spitfire.estec.esa.int/ODI/dplot_SREM.html. The TC2 channel with the energy threshold of about 49 MeV for protons is used in this study. SEPs are removed and daily values are binned into BR-averaged values. It should be noted that the distance of the Rosetta spacecraft swang greatly between 1 and 4.5 AU after 2009 (Honig et al. 2019), and therefore its GCR profile has the spatial gradient effects due to the varying heliospheric distance. The same effect applies for the cruise-phase Cassini spacecraft (blue line in the sixth panel of Fig.1a, from 1 AU to 9.5 AU before July 2004) and the New Horizons data (between 22 and 40 AU). The gradient

of the GCR flux is only about 2%–4% per AU (at distances < 10 AU) according to multi-spacecraft observations (Honig et al. 2019; Roussos et al. 2020). The heliospheric distance for each dot shown in Fig.1b is marked using the distance of the spacecraft when the extremum is identified and extra caution should be taken for those obtained from these distance-changing datasets.

The data from the Cassini spacecraft were obtained through the Low Energy Magnetospheric Measurement System (LEMMS), one of the three energetic particle detectors of the Magnetosphere Imaging Instrument (MIMI) suite (Krimigis et al. 2004, https://pds-ppi.igpp.ucla.edu/search/view/ ?f=yes&id=pds://PPI/CO-S-MIMI-4-LEMMS-CALIB-V1.0). LEMMS is a double-sided energetic particle telescope, with 57 counters designed to measure electrons and ions above several 10 keV and up to about 10 MeV (electrons) and several 100 MeV/n (ions). GCR protons penetrate the shielding of LEMMS and get recorded as a low intensity noise signal, that can be isolated from other magnetospheric or solar wind particle sources, as described in detail in earlier studies (Roussos et al. 2020). The measurements shown here are from LEMMS channel E6 that its GCR response is dominated by >120 MeV protons.

The Pluto Energetic Particle Spectrometer Science Investigation (PEPSSI, McNutt et al. 2008) onboard New Horizon (Stern 2009) were designed to measure keV–MeV pick-up ions from Pluto's outgassing atmosphere. Recently, the channels which were originally used to detect <MeV Jovian electrons have been successfully used to approximate the deep space GCR fluxes (Hill et al. 2020) and the data are described and accessible here http://sd-www.jhuapl.edu/pepssi/analysis/reducedData/. The channel corresponding to ions between 120 MeV and 1.4 GeV is used in this analysis. A few SEP events are removed and daily values are binned into BR-averaged values.

## B. COMPARISON BETWEEN WSO AND HMI/MDI SYNOPTIC CHARTS

Compared to the magnetograms from space-borne instruments, e.g., the SOHO/MDI and the SDO/HMI, which provide the synoptic charts with the resolution of 3600 by 1080 and 3600 by 1440 in Cycles 23 and 24, respectively, the spatial resolution of WSO data is too low. However, MDI data just covered the period from 1996 to 2010, and HMI data from 2010 to date. Thus, we use WSO data for the long-term analysis here. But we also check if the low resolution of WSO data has any influence on the coronal magnetic field extrapolation and consequently affects the statistical results. To do so, we apply the same procedures on the MDI and HMI synoptic charts (http://soi.stanford.edu/magnetic/ index6.html and http://jsoc.stanford.edu/HMI/LOS_Synoptic_charts.html, respectively) to derive the open flux, open area and the open field strength.

Here, we reduce the spatial resolution of the MDI and HMI data to 360 by 180, calculate the spherical harmonic coefficients up to 180 orders, and trace field lines at a 180 by 90 mesh to save the computing time. These reduce synoptic charts are 30 time higher in resolution than WSO charts. Figure A2 shows the solar cycle variations of the open area and open flux based on the MDI and HMI data. Their variation patterns look almost the same as those displayed in Figure 4, except that the absolute values are different. The open area derived based on the WSO data is larger than that based on the MDI and HMI data, whereas the open flux based on the WSO data is smaller. The correlation between the WSO and MDI/HMI data is displayed in Figure A3. It can be found that the slopes of the fitting lines obviously deviate from unity, suggesting that the open flux based on the WSO data is about 4-5 times smaller than that based on the MDI and HMI data, the open area is about 2-3 times larger, and the averaged open field strength is about 20 times smaller. But the correlation coefficients of the open flux, open area and the open field strength are as high as 0.88,
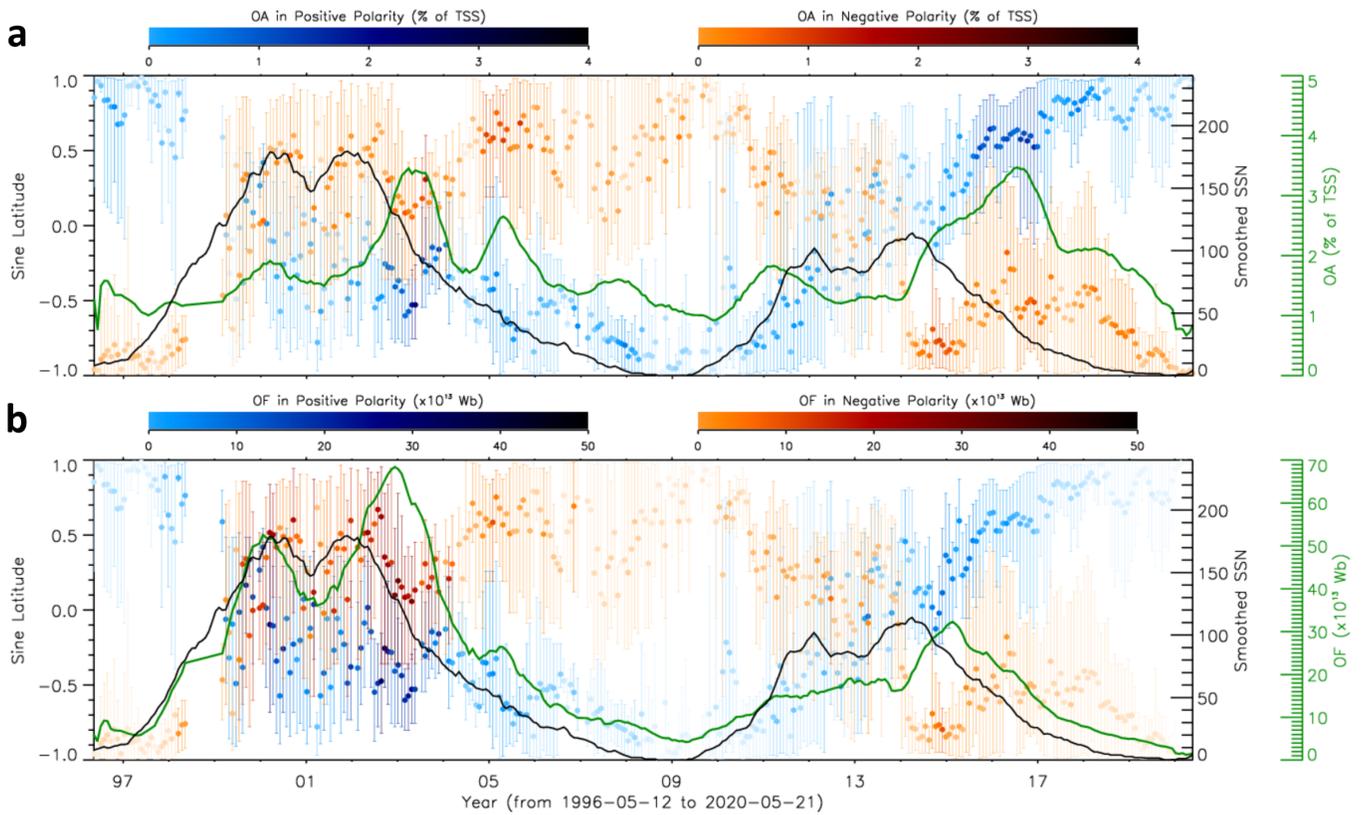
Figure A2. Similar to Fig.4. The data points before 2011 June 25, which is the beginning of BR 2414, are derived based on the MDI synoptic charts, and those after 2011 June 25 are obtained based on the HMI synoptic charts.

0.76 and 0.74, respectively, suggesting the parameters derived from WSO data are well correlated with those from the MDI and HMI data. Thus, the low spatial resolution of the WSO data should not distort the statistical results presented in the main text.
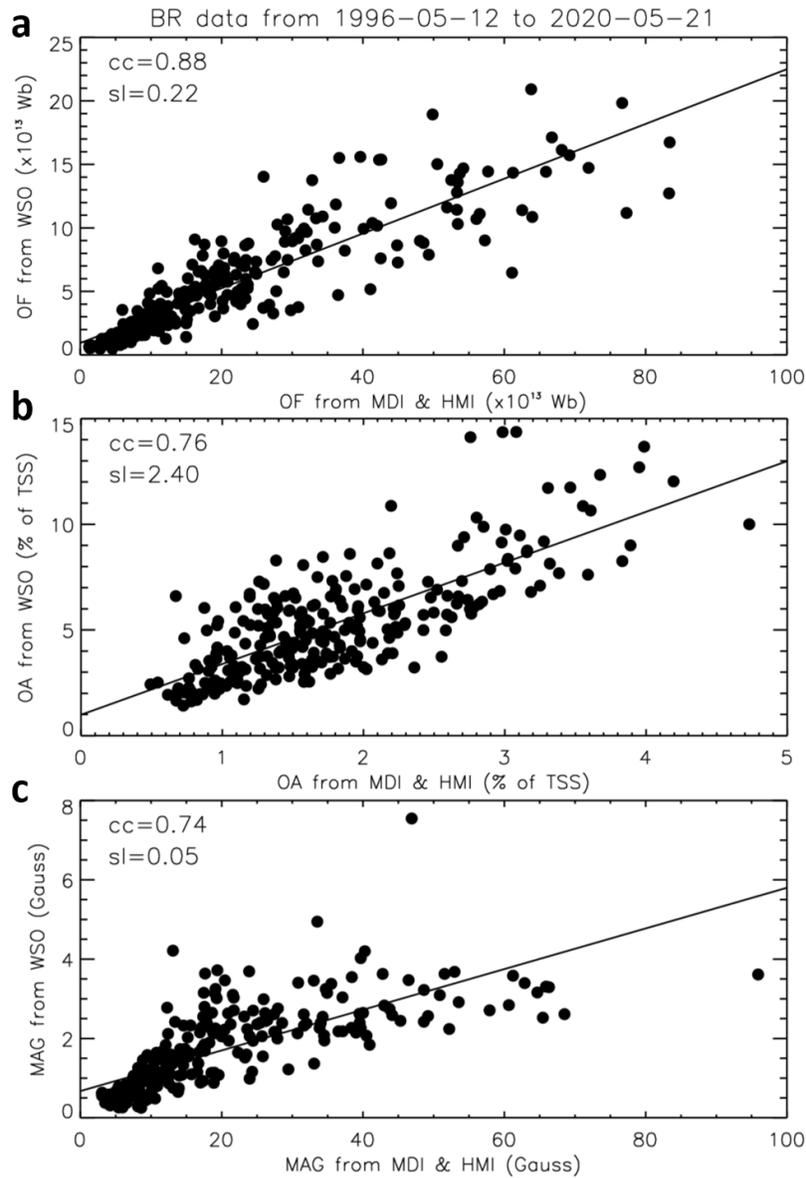
Figure A3. The scatter plots showing the correlation between the parameters derived based on the WSO data and those based on the MDI and HMI data during 1996 – 2020.

REFERENCES

Alanko-Huotari, K., Usoskin, I., Mursula, K., &
    Kovaltsov, G. 2007, Adv. in Space Res., 7, 1064

Boynton, W. V., Feldman, W., Mitrofanov, I.,
    et al. 2004, Space Sci. Rev., 110, 37

Brueckner, G. E., Howard, R. A., Koomen, M. J.,
    et al. 1995, Sol. Phys., 162, 357

Clette, F., Svalgaard, L., Vaquero, J. M., &
    Cliver, E. W. 2014, Space Sci. Rev., 186, 35

Cliver, E. W., & Ling, A. G. 2001, Astrophys. J.
    Lett., 551, L189

Cucinotta, F. A., To, K., & Cacao, E. 2017, Life
    Sci. and Space Res., 13, 1,
    doi: 10.1016/j.lssr.2017.01.005

Domingo, V., Fleck, B., & Poland, A. I. 1995,
    Space Sci. Rev., 72, 81

Dorman, L. I. 2001, Adv. Space Res., 27, 601

Duvall, T. L. J., Wilcox, J. M., Svalgaard, L.,
    Scherrer, P. H., & McIntosh, P. S. 1977, Sol.
    Phys., 55, 63

Evans, H., Bühler, P., Hajdas, W., et al. 2008,
    Adv. in Space Res., 42, 1527

Ferreira, S., & Potgieter, M. 2004, Astrophys. J.,
    603, 744

Glassmeier, K.-H., Boehnhardt, H., Koschny, D.,
    Kührt, E., & Richter, I. 2007, Space Sci. Rev.,
    128, 1

Gui, B., Shen, C., Wang, Y., et al. 2011, Sol.
    Phys., 271, 111

Guo, J., Zeitlin, C., Wimmer-Schweingruber,
    R. F., et al. 2018, Astron. J., 155, 49

Hassler, D. M., Zeitlin, C.,
    Wimmer-Schweingruber, R. F., et al. 2012,
    Space Sci. Rev., 170, 503

—. 2014, Science, 343, 1244797

Hill, M. E., Allen, R. C., Kollmann, P., et al.
    2020, Astrophys. J., 905, 69

Hoeksema, J. T., Liu, Y., Hayashi, K., et al. 2014,
    Sol. Phys., 289, 3483

Honig, T., Witasse, O. G., Evans, H., et al. 2019,
    Annales Geophysicae, 37, 903

Jiang, J., Cameron, R. H., Schmitt, D., &
    Schüssler, M. 2011, Astron. & Astrophys., 528,
    A83

Jokipii, J., Levy, E., & Hubbard, W. 1977,
    Astrophys. J., 213, 861

Jokipii, J. R., Kota, J., Giacalone, J., Horbury,
    T. S., & Smith, E. J. 1995, Geophys. Res. Lett.,
    22, 3385

Krimigis, S., Decker, R., Roelof, E., et al. 2013,
    Science, 341, 144

Krimigis, S. M., Mitchell, D. G., Hamilton, D. C.,
    et al. 2004, Space Sci. Rev., 114, 233

Luhmann, J. G., Gosling, J. T., Hoeksema, J. T.,
    & Zhao, X. 1998, J. Geophys. Res.: Space
    Phys., 103, 6585

McNutt, R. L., Livi, S. A., Gurnee, R. S., et al.
    2008, Space Sci. Rev., 140, 315

Moloto, K., & Engelbrecht, N. E. 2020, The
    Astrophysical Journal, 894, 121

Müller-Mellin, R., Kunow, H., Fleißner, V., et al.
    1995, Solar Physics, 162, 483,
    doi: 10.1007/978-94-009-0191-9_13

Nagashima, K., & Morishita, I. 1980, Planet.
    Space Sci., 28, 177

Owens, M. J., & Crooker, N. U. 2006, J. Geophys.
    Res.: Space Phys., 111, A10104

Parker, E. N. 1965, Planet. Space Sci., 13, 9,
    doi: 10.1016/0032-0633(65)90131-5

Pesnell, W. D., Thompson, B. J., & Chamberlin,
    P. C. 2012, Sol. Phys., 275, 3

Potgieter, M. 1998, Space Sci. Rev., 83, 147

Potgieter, M. S. 2013, Living Rev. Sol. Phys., 10, 1

Robbrecht, E., & Berghmans, D. 2004, Astron. &
    Astrophys., 425, 1097,
    doi: 10.1051/0004-6361:20041302

Ross, E., & Chaplin, W. J. 2019, Sol. Phys., 294, 8

Rouillard, A., & Lockwood, M. 2004, Annales
    Geophysicae, 22, 4381

Roussos, E., Dialynas, K., Krupp, N., et al. 2020,
    Astrophys. J., 904, 165

Scherrer, P. H., Bogart, R. S., Bush, R. I., et al.
    1995, Sol. Phys., 162, 129

Schrijver, C. J., & Derosa, M. L. 2003, Sol. Phys.,
    212, 165

Shen, Z., Qin, G., Zuo, P., Wei, F., & Xu, X.
    2020, The Astrophysical Journal, 900, 143

Stern, S. A. 2009, New Horizons, 3

Temmer, M., Veronig, A., & Hanslmeier, A. 2003,
    Sol. Phys., 215, 111

Thomas, S. R., Owens, M. J., & Lockwood, M.
    2014, Sol. Phys., 289, 407

Usoskin, I., Alanko-Huotari, K., Kovaltsov, G., &
    Mursula, K. 2005, J. Geophys. Res.: Space
    Phys., 110, A12108

Usoskin, I., Kananen, H., Mursula, K., Tanskanen,
    P., & Kovaltsov, G. 1998, J. Geophys. Res.:
    Space Phys., 103, 9567

Usoskin, I., Mursula, K., Kananen, H., &
    Kovaltsov, G. 2001, Advances in Space
    Research, 27, 571

Van Allen, J. A. 2000, Geophys. Res. Lett., 27,
    2453

Wang, Y., & Zhang, J. 2007, Astrophys. J., 665,
    1428

Wang, Y.-M., Hawley, S. H., & Sheeley, N. R.
    1996, Science, 271, 464

Wang, Y.-M., Lean, J. L., & Sheeley, Jr., N. R.
    2005, Astrophys. J., 625, 522

Webber, W. R., & Lockwood, J. A. 1988, J.
    Geophys. Res.: Space Phys., 93, 8735

Wheatland, M., & Litvinenko, Y. E. 2001,
    Astrophys. J., 557, 332

Yashiro, S., Gopalswamy, N., Michalek, G., et al.
    2004, J. Geophys. Res.: Space Phys., 109,
    A07105

Zhao, X., & Hoeksema, J. T. 1995, J. Geophys.
    Res.: Space Phys., 100(A1), 19